PARTICLE IMAGE VELOCIMETRY AND PROPER ORTHOGONAL DECOMPOSITION ANALYSIS OF THE CHANNEL FLOW EQUIPPED WITH CYLINDRICAL RIBS

by

Cahit GURLEK *

Department of Mechanical Engineering, University of Cumhuriyet, Sivas, Turkey

Original scientific paper
https://doi.org/10.2298/TSCI170305204G

The characteristics of the flow fields in a rectangular channel equipped with cylindrical ribs were examined through the particle image velocimetry experiments. The mean and turbulence characteristics were presented for three different Reynolds numbers of 2900, 8400, and 15000. In addition, the coherent flow structures were extracted by means of the proper orthogonal decomposition method. The flow field is characterized by a large re-circulation region and a secondary clockwise-rotating corner vortex. The high vorticity, fluctuation velocity and shear stress contours are formed along the free shear layers emanating from the upstream rib. As Reynolds numbers increase, the positive vorticity contours extend downstream and fluctuation velocity and shear stress contours spread out towards the channel wall. The proper orthogonal decomposition results have shown that a horizontally aligned co-rotating vortex pair and a corner vortex are the dominant flow structures for the highest Reynolds number.

Key words: *channel flow, cylindrical ribs, proper orthogonal decomposition, flow separation, particle image velocimetry*

Introduction

Ribbed channels have been the subject of various numerical and experimental investigations because of their relevance in many fluid engineering fields that include heat exchangers, solar air heaters, cooling of turbine blades and vanes, electronic devices, nuclear reactors, *etc*. [1-5]. The main idea is augmenting the mixing, and hence the heat transfer, with disturbance of flow field by attaching rib arrays onto a channel surface.

Rib shape is one of the most important geometrical parameters affecting the heat transfer mechanisms in a ribbed channel, and the others can be summarized: rib-pitch-to-rib--height ratio, rib-height-to-channel-height ratio, channel aspect ratio, and rib angle-of-attack.

Numerous early studies have essentially concentrated on square (or rectangular) shaped ribs and investigated the effects of aforementioned geometrical parameters on the heat and flow performance [6-15]. Several investigations comparing different shaped ribs have been performed in order to identify the shape effect on the heat transfer mechanism for ribbed channels. The common rib geometries which have been investigated are triangular, semi-cylindrical, cylindrical, trapezoidal, *etc*. A detailed review can be found in Varun *et al*. [16]. Tauscher and Mayinger [17] obtained the temperature and velocity fields in the heat exchanger channel roughened by various shaped ribs experimentally. They found that the circular ribs

* Author's e-mail: cgurlek@cumhuriyet.edu.tr

showed the best heat transfer performance at all Reynolds numbers ranging from 500-5000. Kilicaslan and Sarac [18] performed an experimental study to examine the effect of the cylindrical and triangular ribs on the enhancement of heat transfer in a compact heat exchanger. They concluded that cylindrical ribs provided a higher heat transfer rate than triangular ribs. Chaube *et al*. [19] carried out a numerical study of heat transfer augmentation and flow characteristics of a rectangular duct for Reynolds numbers between 3000 and 20000. They examined nine different shapes of ribs and reported that the circular and semi-circular ribs showed good friction performance but gave lower heat transfer enhancement than other rib shapes. Wongcharee *et al*. [20] investigated the heat and fluid-flow characteristics of a rectangular channel equipped with various shaped ribs including cylindrical configuration, numerically. They found that the cylindrical rib provided the highest thermal enhancement factor. Chung *et al*. [21] analyzed the thermal and flow characteristics of a channel roughened with different shaped ribs for the Reynolds numbers in the range between 19800 and 24200. The Nusselt number ratio increased with increasing Reynolds numbers, and values of this ratio for semi-circular ribs were higher than square ribs. Luo *et al*. [22] numerically studied the effects on heat transfer and friction factor of the combination of delta-winglet vortex generators and different obstacles for a solar receiver heat exchanger. The results showed that the perturbation of the semi-cylinder ribs provided the highest heat transfer augmentation. Alfarawi *et al*. [23] investigated the heat transfer and flow friction characteristics in a rectangular duct roughened by semi-circular, rectangular and hybrid of semi-circular and rectangular shapes. It was found that the hybrid ribs provided higher values for the efficiency indices than those of the rectangular and semi-circular ribs cases.

Based on the open literature, cylindrical shaped ribs are useful in enhancing heat transfer. However, the previous studies have mostly highlighted the heat transfer characteristics. Therefore, the main objective of the present study is to depict the flow features of a rectangular channel roughened with cylindrical ribs by means of particle image velocimetry (PIV) and proper orthogonal decomposition (POD) techniques.

Experimental arrangements

An illustrative diagram of the ribbed channel with a square cross-section of 150 mm × 150 mm is depicted in fig. 1. Ten circular cross-section ribs with a diameter of 50 mm were mounted on one wall in the second half of the channel. They were placed orthogonally to the flow direction. The ribs were constructed from aluminum tubes and covered with a thin black coating to avoid the reflected laser. Geometrical features: rib-pitch-to-rib-diameter ratio (P/d) and hydraulic-diameter-to-rib-diameter ratio (D_h/d) were both 3. Although it has a comparatively low heat transfer performance, the rib configuration used in this study (rib spacing of P/d smaller than 4) has been studied extensively [24].

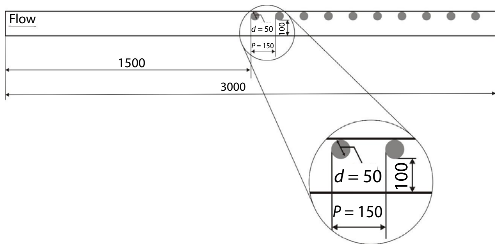

Figure 1. Schematic diagram of the ribbed channel

A graphical representation of the experimental configuration and co-ordinate system used in this research is presented in fig. 2. Here, x, y, and z refer to the stream-wise, vertical (positive in upward) and cross-stream directions, respectively. The measurements were performed in a closed-loop open-water channel with a test section of 750 mm (height) × 1000 mm (width) × 8000 mm (length) and a turbulence level of less than 0.5%. The flow was circulated by a centrifugal pump, and free-stream velocities were adjusted using a speed control module. The ribbed channel was immersed and located on a flat elevated surface in water channel. The measurements were made at three Reynolds numbers of 2900, 8400, and 15000 based on the mean velocities, U_m, and the hydraulic diameter of the ribbed channel, D_h. The U_m velocities were obtained by averaging the stream-wise velocities along a vertical centerline of the ribbed channel located at a distance of 9 D_h downstream from the channel inlet. The related velocity profiles are displayed in fig. 3.

Instantaneous velocity field measurements were conducted using a 2-D Dantec PIV system. Measurements were performed for the flow field bounded by the eighth and ninth ribs on the vertical symmetry plane z = 0. A double pulsed Nd:YAG laser (120 mJ at 532 nm) was used for illuminating the measurement area. The flow was seeded by silver coated hollow glass spheres with a mean particle diameter of 10 μm. The particle images were recorded by a high-speed CCD camera with a sensor resolution of 1600 × 1200 pixel. The spatial resolution was about 0.13 mm/pixel. The interrogation window sizes were 32 × 32 pixels with a 50% overlap. The flow patterns were obtained by using a FFT based algorithm via the FLOW MAP software. For each measurement, 350 pairs of images were recorded with a sampling rate of 15 Hz and ensemble-averaged to obtain the mean flow field properties. Each measurement was repeated three times to check the repeatability of the experiments. Figure 4 shows a typical replicate velocity profiles for Re = 8400. Similar reproducibilities were observed in the repeated measurements conducted for different Reynolds numbers. The PIV measurement uncertainties were calculated using the method described by

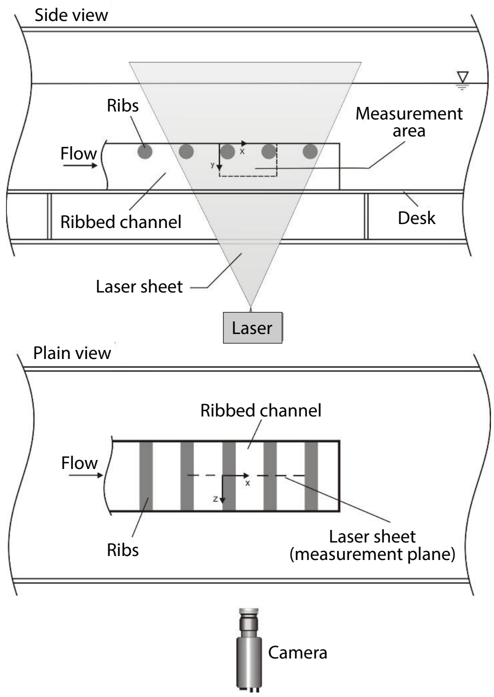

Figure 2. Schematic diagram of the experimental set-up

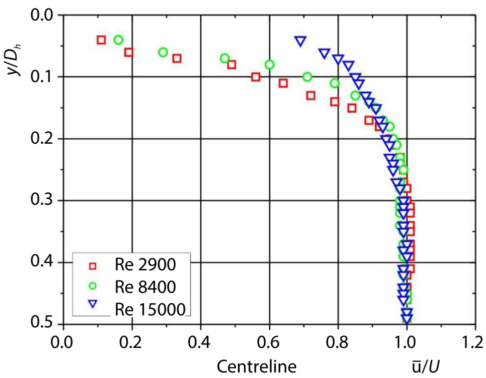

Figure 3. Mean inlet velocity profiles

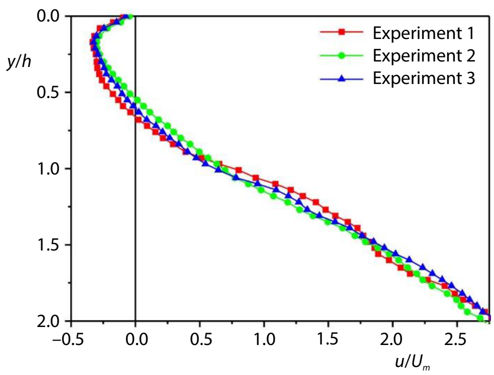

Figure 4. Test of experimental repeatability for stream-wise velocity profiles at x/h = 2

Lo *et al*. [25] which considers the three main sources of uncertainties including: the error from the software correlation, the accuracy of the seeding particles to follow the fluid flow and the uncertainty in velocity measurement using PIV. The corresponding overall uncertainty of the PIV measurements was about 4%.

Proper orthogonal decomposition

The POD is a statistical tool that has been used widely to identify coherent structures in fluid-flow applications and was first applied in the related context by Lumley [26]. Coherent structures are well-defined dynamical patterns in the flow fields on large and intermediate scales that appear systematically. They contain energy and have a significant effect on mixing and heat transfer and, therefore, their identification is important. The POD takes a series of instantaneous snapshots as input and extracts *POD modes* which depict the organized structures having maximum turbulent kinetic energy. In this study the *snapshot POD* approach was used to identify the POD modes [27]. Analyses were performed by using Dynamic Studio 2015a software. More details and the mathematical background can be found in [28].

Results and discussion

Figures 5 and 6 show the mean velocity vector fields, $\bar{v}$, and the streamline patterns $\bar{\psi}$, respectively, in the measurement plane for three Reynolds numbers. In fig. 6, the cores of re-circulating regions are denoted with F_1 and F_2. For all Reynolds numbers, the separating flow from the upper surface of the downstream rib forms a large circulation region which spans the entire flow field bounded by the cylindrical ribs. With increasing Reynolds numbers, a small secondary separation bubble (Moffat eddy) rotating in the opposite direction to the primary re-circulation one emerges adjacent to the downstream rib which originates from the detachment of flow from the channel wall.

The distance between the primary re-circulation regions and the channel wall changes with the Reynolds numbers and it is larger than that of the others for Re = 8400. Stream lines

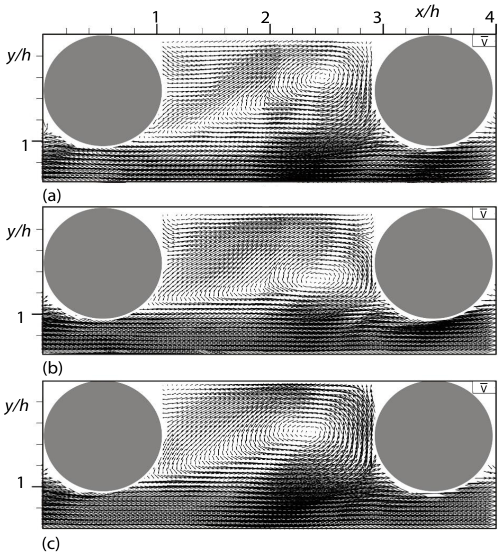

Figure 5. Mean velocity vector fields; (a) Re = 2900, (b) Re = 8400, and (c) Re = 15000

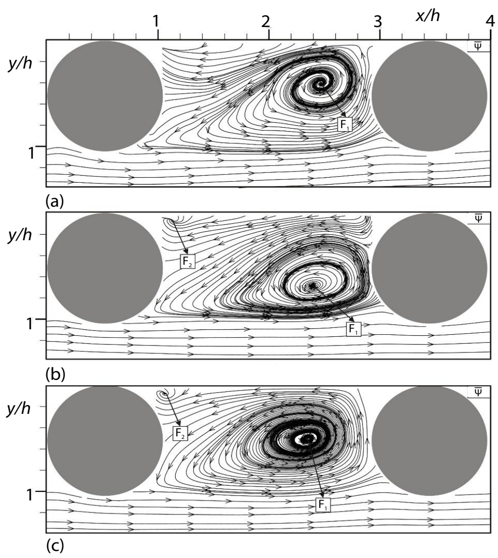

Figure 6. Mean streamline patterns; (a) Re = 2900, (b) Re = 8400, and (c) Re = 15000

are nearly parallel outside of the primary re-circulation zone. As can be clearly seen in fig. 6, low heat transfer performance of this rib configuration, which was mentioned earlier, are caused by the trapped re-circulating flow between the cylindrical ribs. The general behavior of the flow patterns is very similar to those previously depicted in a solar heater with cylindrical ribs [29]. Figure 7 shows the time-averaged stream-wise velocity contours, $\bar{u}/U_m$, between the cylindrical ribs with varying Reynolds numbers. The re-circulation regions which are evident from the negative values of stream-wise velocity occupy the upper part of the entire flow region between the ribs. The maximum height of the re-circulation region close to the second rib is observed for the Reynolds number of 8400.

The mean contour plots of vorticity, $\bar{\omega}$, are shown in fig. 8 (the contour line interval is 0.2 s^{-1}). The solid lines represents positive (counterclockwise) and dashed lines represents negative (clockwise) values of vorticity contours. The concentrated longitudinal positive vorticity contours apparently oriented within the free shear layers emanating from the lower edge of the upstream rib. A pair of positive circular vortices is observed close to the downstream rib. As Reynolds numbers increase, the positive longitudinal vorticity separating from the upstream rib extends downstream and eventually merges with aforementioned pair of vortices. There is also an attached clockwise negative wall vorticity noticeable between the ribs, which gets relatively stronger with increasing Reynolds numbers.

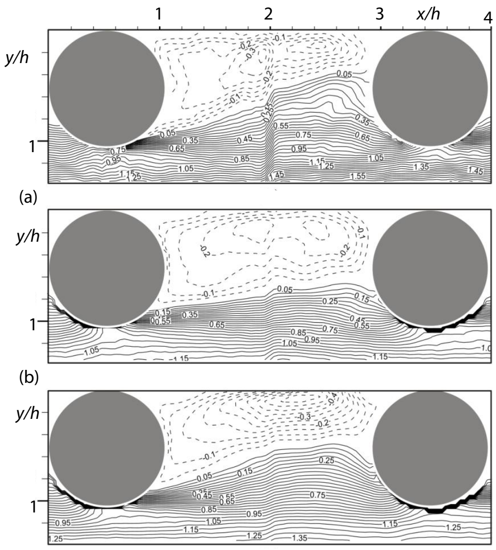

Figure 7. Contours of non-dimensional mean stream-wise velocity; (a) Re = 2900, (b) Re = 8400, and (c) Re = 15000

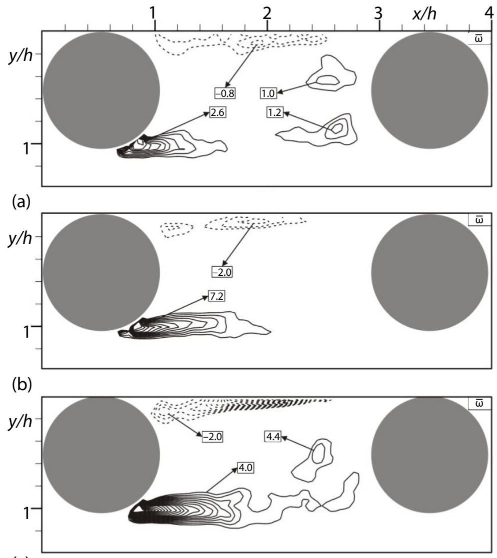

Figure 8. Contours of mean vorticity; (a) Re = 2900, (b) Re = 8400, and (c) Re = 15000, $\Delta\bar{\omega}$ = 0.2 s^{-1}

The contours of the normalized root-mean-square (RMS) fluctuation velocity, u_{rms}/U_m, are depicted in fig. 9 (the contour line interval is 0.025). The higher magnitude of RMS fluctuation velocity contours are formed along the free shear layer originating from the upstream ribs. The RMS velocity contours elongate up to the downstream rib. With increasing Reynolds numbers, u_{rms}/U_m contours spread toward the channel wall and eventually occupy the whole region between the ribs. It is also worth mentioning that the turbulent kinetic energy contours, not presented here, show similar distributions to the RMS velocity contours.

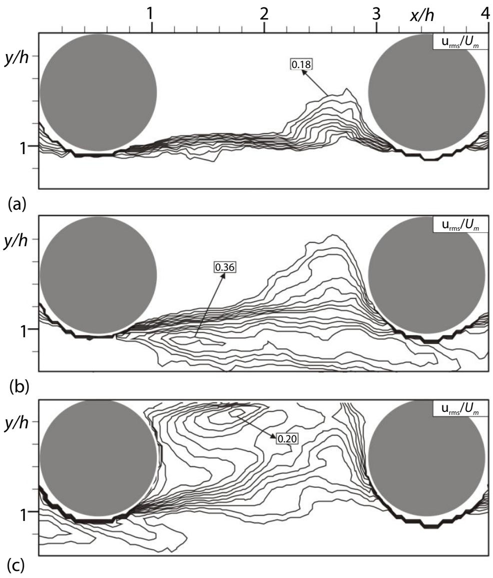

Figure 9. Contours of stream-wise velocity fluctuations; (a) Re = 2900, (b) Re = 8400, and (c) Re = 15000, $\Delta[u_{rms}/U_m]$ = 0.025

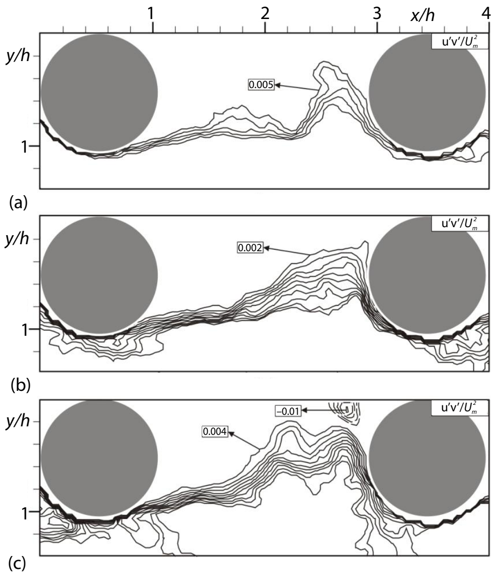

Figure 10. Contours of shear stresses; (a) Re = 2900, (b) Re = 8400, and (c) Re =15000, $\Delta[u'v'/U_m^2]$ = 0.005

Figure 10 presents the normalized Reynolds shear stress contours, $u'v'/U_m^2$ (the contour line interval is 0.005). The high shear stress levels intensify near the free shear layers and extend between the cylindrical ribs. It can be seen also that with increasing Reynolds numbers, the $u'v'/U_m^2$ contours spread out vertically towards the channel wall. Turbulence intensity and Reynold stresses characteristics show some similarities with the channel flow roughened by rectangular ribs with high aspect and blockage ratio [10].

Time-dependent flow features of streamlines for the Reynolds number, 15000 are shown in fig. 11. Despite the flow structure similar to the mean flow appears in some instantaneous images, the flow field is quite different and complex. The vortex pairs with horizontal alignments are clearly visible and their size changes in time, alternately. They move towards each other, combine and eventually form a large-scale re-circulation region. In addition, the animation of instantaneous velocity vector fields display the trapped structure of the main circulation region between the cylindrical ribs, clearly.

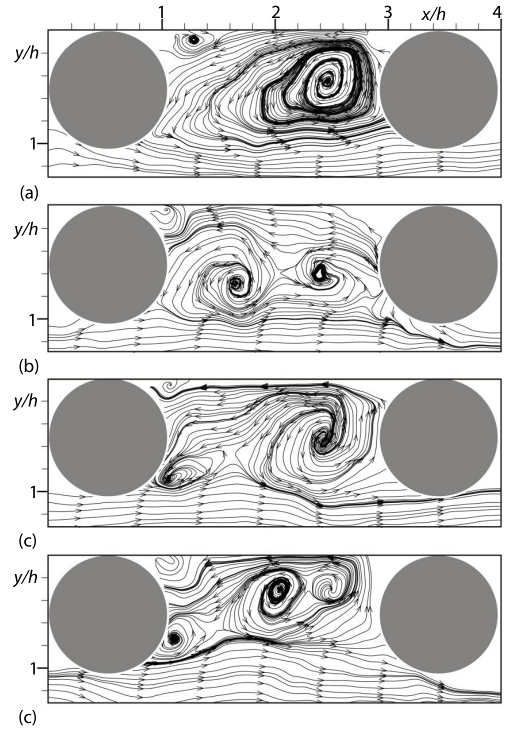

Figure 11. Instantaneous streamline patterns at Re = 15000; (a) image number N = 11, (b) N = 41, (c) N = 59, and (d) N = 246

Figure 12 shows the mean velocity profiles in the measurement plane $z = 0$. Figure 12(a) represents the normalized mean stream-wise velocity profiles, $\overline{u}/U_m$, at the stream-wise location $x/h = 2$ for the tree Reynolds numbers. The stream-wise velocities were normalized by the associated mean velocities, U_m, for each Reynolds number. The velocity profiles in the near wall region exhibit negative values that indicates the reverse flow, apparently. These reverse flow regions are visible up to $y/h = 0.7$ for Re = 2900, and $y/h = 0.5$ for both Re = 8400 and 15000. In addition, peak values occur in the vicinity of the channel wall. The positive velocity profiles are almost identical up to $y/h = 1.4$ for all Reynolds numbers. Starting from this point the velocity profile at Re = 2900 displays a different trend. Figure 12(b) shows the normalized mean stream--wise velocity profiles, $\overline{u}/U_m$, along the axis connecting the center of cylinders ($y/h = 0.5$) between $x/h = 1$ and 3. Velocity profile of Re = 2900 have an almost sinusoidal shape with negative and positive peak values of –0.27 and 0.21, respectively. For Re = 8400, the flow is totally reversed along the measurement axis. As can be seen in figure, at Re =15000 the velocity profile exhibits an asymmetric sinusoidal shape with relatively small positive values.

The fluctuation velocity and shear stress profiles corresponding to the mean flow data at $x/h = 2$ are displayed in fig. 13. The normalized RMS velocity profiles, u_{rms}/U_m, are displayed in fig. 13(a). As expected, for all Reynolds numbers, peak values arise within the shear layer. For Re = 2900, the RMS velocity distribution deviates from the others after $y/h = 0.35$ with two peak values of 0.65 and 0.67. The profiles of RMS velocities for

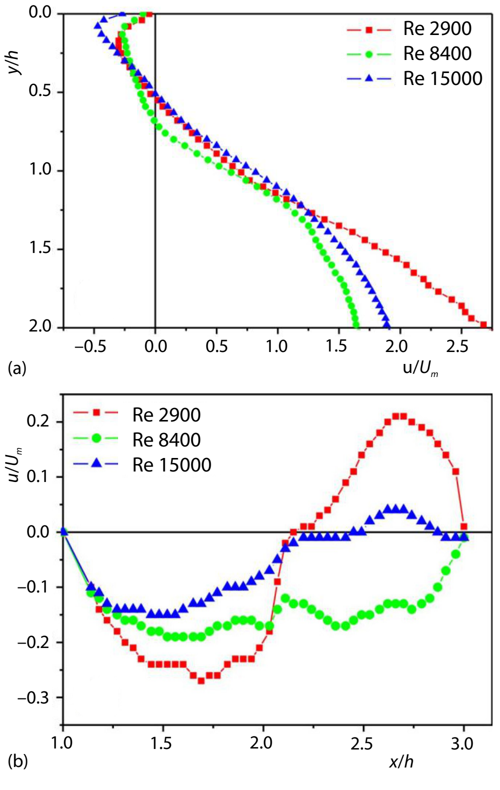

Figure 12. Mean stream-wise velocity profiles; (a) $x/h = 2$ and (b) $y/h = 0.5$

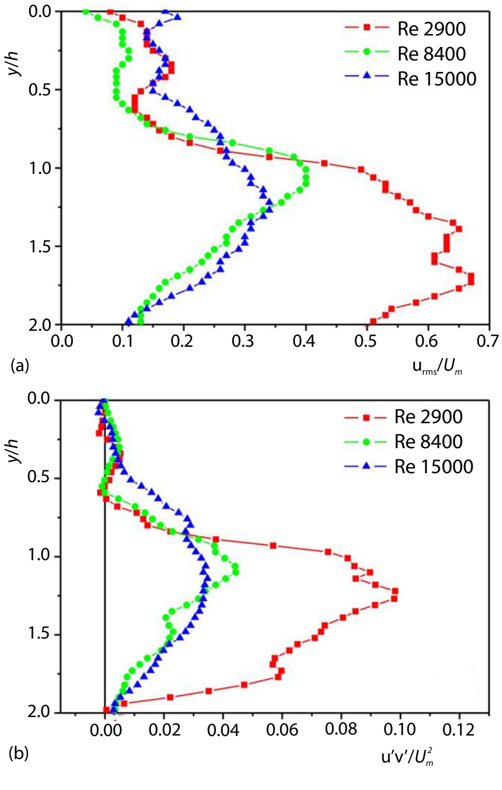

Figure 13. Profiles of (a) stream-wise velocity fluctuations and (b) shear stresses

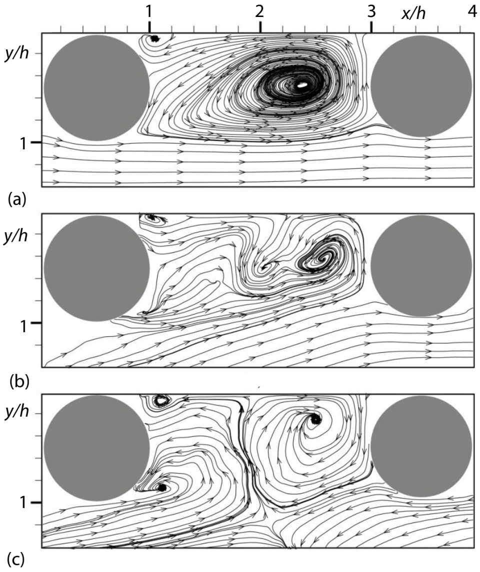

Figure 14. The POD modes; (a) mode zero, (b) 1st mode, and (c) 2nd mode

Re = 8400 and Re =15000 follow nearly triangular shaped profiles with maximum values of 0.4 and 0.34, respectively. As it can be seen later, the overall characteristics of RMS velocity profiles are mirrored by those of the shear stresses. Normalized Reynolds shear stress profiles, $u'v'/U_m^2$, are provided in fig. 13 (b) where it indicates that the shear stresses are very low in the near-wall region for all Reynolds numbers. For Re = 2900 and 8400 $u'v'/U_m^2$ profiles behave similarly up to y/h = 1.4. It can be seen that after y/h = 1.4 the shear stress profile for Re = 2900 is clearly different from that of others having a peak value of 0.098. In the far-wall region (y/h > 0.5), $u'v'/U_m^2$ profiles tend to approach triangular and parabolic shapes for Re = 8400 and 15000, respectively, with comparable maximum values of 0.044 and 0.035.

The first three POD modes for Re = 15000 which are depicted by streamlines are presented in fig. 14. Note that the mode zero represents the mean velocity field, fig. 6(a). The 1st and 2nd POD modes (the first two most energetic POD modes) contain 15% and 10% of kinetic energy of the flow, respectively. It can be identified from the first POD mode that a horizontally aligned co-rotating vortex pair and a Moffat eddy are the dominant flow structures. Two large counter rotating vortices close to ribs and a Moffat eddy are the main flow characteristics of the second POD mode.

Conclusion

The flow structures of a rectangular channel equipped with cylindrical ribs have been investigated experimentally. The mean and instantaneous flow features and turbulent statistics have been depicted for three different Reynolds numbers through PIV measurements. In addition, the organized structures having maximum fluctuation energy have been extracted by means of POD method. The collected experimental data could contribute to numerical model validations.

Nomenclature

d – diameter of cylindrical rib, [mm]
D_h – hydraulic diameter of the ribbed channel, [mm]
h – height of the ribbed channel, [mm]
N – image number, [–]
P – rib pitch, [mm]
Re – Reynolds number ($=U_m D_h/\nu$), [–]
u – stream-wise velocity [mms^{-1}]
U_m – stream-wise mean velocity [mms^{-1}]
u_{rms} – stream-wise turbulence intensity [mms^{-1}]
u'v' – Reynolds stress correlation, [mm^{2}s^{-2}]
$\bar{u}$ – time averaged axial velocity (along x-co-ordinate)
$\bar{v}$ – time averaged lateral velocity (along y-co-ordinate)
$\bar{V}$ – time averaged total velocity vector, [mms^{-1}]
x, y, z – Cartesian co-ordinates

Greek symbols

ν – kinetic viscosity, [mms^{-2}]
$\bar{\psi}$ – time averaged streamline, [–]
$\bar{\omega}$ – time averaged vorticity, [s^{-1}]

References

[1] Tauscher, R., Mayinger, F., Heat Transfer Enhancement in a Plate Heat Exchanger with Rib-Roughened Surfaces, in: *Heat Transfer Enhancement of Heat Exchangers*, (Eds. S., Kakac, *et al.*) Kluwer Academic Publishers, Boston, Mass., USA, 1999, pp. 207-221
[2] Verma, S. K., Prasad, B. N., Investigation for the Optimal Thermohydraulic Performance of Artificially Roughened Solar Air Heaters, *Renewable Energy, 20* (2000), 1, pp. 19-36
[3] Son, S. Y., *et al*., PIV Flow Measurements for Heat Transfer Characterization in Two-Pass Square Channels with Smooth and 90° Ribbed Walls, *Int. J. Heat Mass Transfer, 45* (2002), pp. 4809-4822
[4] Sivasankaran, H., *et al*., Experimental Analysis of Parallel Plate and Crosscut Pin Fin Heat Sinks for Electronic Cooling Applications, *Thermal Science, 14* (2010), 1, pp. 147-156
[5] Keshmiri, A., Three-Dimensional Simulation of a Simplified Advanced Gas-cooled Reactor Fuel Element, *Nuclear Engineering and Design, 241* (2011), 10, pp. 4122-4135
[6] Lorenz, S., *et al*., Distribution of the Heat Transfer Coefficient in a Channel with Periodic Transverse Grooves, *Exp. Thermal and Fluid Science, 11* (1995), 3, pp. 234-242
[7] Han, J. C., Park, J. S., Developing Heat Transfer in Rectangular Channels with Rib Turbulators, *Int. J. Heat Mass Transfer, 31* (1988), 1, pp. 183-195
[8] Yang, K., Large Eddy Simulation of Turbulent Flows in Periodically Grooved Channel, *Journal Wind Engineering, 84* (2000), 1, pp. 47-64
[9] Cui, J., *et al*., Large-Eddy Simulation of Turbulent Flow in a Channel with Rib Roughness, *Int. J. Heat and Fluid Flow, 24* (2003), 3, pp. 372-388
[10] Casarsa, L., Arts, T., Experimental Investigation of the Aerothermal Performance of a High Blockage Rib-Roughened Cooling Channel, *ASME J. Turbomachinery, 127* (2005), 3, pp. 580-588
[11] Hyun, B. S., *et al*., Turbulent Flow over Two-Dimensional Rectangular-Shaped Roughness Elements with Various Spacings, *Proceedings*, MTS/IEEE OCEANS Conference, Singapore, 2007, pp. 1-6
[12] Wang, L., *et al*., PIV Measurements of Separated Flow in a Square Channel with Streamwise Periodic Ribs on One Wall, *ASME J. Fluids Engineering, 129* (2007), 7, pp. 834-841
[13] Wang, L., *et al*., Turbulent Flow in a Ribbed Channel: Flow Structures in the Vicinity of a Rib, *Exp. Thermal and Fluid Science, 34* (2010), 2, pp. 165-176
[14] Cardwell, N. D., *et al*., Developing and Fully Developed Turbulent Flow in Ribbed Channels, *Exp. Fluids, 50* (2011), 5, pp. 1357-1371
[15] Coletti, F., *et al*., Flow Field Investigation in Rotating Rib-Roughened Channel by Means of Particle Image Velocimetry, *Exp. Fluids, 52* (2012), 4, pp. 1043-1061
[16] Varun, Saini, R. P., Singal, S. K., A Review on Roughness Geometry Used in Solar Air Heaters, *Solar Energy, 81* (2007), 11, pp. 1340-1350
[17] Tauscher, R., Mayinger, F., Enhancement of Heat Transfer in a Plate Heat Changer by Turbulence Promotors, in: *Compact Heat Exchangers for the Process Industries*, (Ed. R. K., Shah), Begell House, New York, USA, 1997, pp. 253-260
[18] Kilicaslan, I., Sarac, H. I., Enhancement of Heat Transfer in Compact Heat Exchanger by Different Type of Rib with Holographic Interferometry, *Exp. Thermal and Fluid Science, 17* (1998), 4, pp. 339-346
[19] Chaube, A., *et al*., Analysis of Heat Transfer Augmentation and Flow Characteristics Due to Rib Roughness over Absorber Plate of a Solar Air Heater, *Renewable Energy, 31* (2006), 3, pp. 317-331
[20] Wongcharee, K., *et al*., Numerical Investigation of Flow Friction and Heat Transfer in a Channel with Various Shaped Ribs Mounted on Two Opposite Ribbed Walls, *Int. J. Chem. Reactor Eng., 9* (2011), 1, pp. 1-22
[21] Chung, H. S., *et al*., Study on the Thermal and Flow Characteristics on the Periodically Arranged Semi-Circular Ribs in a Rectangular Channel, *Exp. Heat Transfer, 27* (2014), 1, pp. 56-71
[22] Luo, L., *et al*., Thermal Enhancement by Using Grooves and Ribs Combined with Delta-Winglet Vortex Generator in a Solar Receiver Heat Exchanger, *Applied Energy, 183* (2016), Dec., pp. 1317-1332
[23] Alfarawi, S., *et al*., Experimental Investigations of Heat Transfer Enhancement from Rectangular Duct Roughened by Hybrid Ribs, *Inter. J. Thermal Sciences, 118* (2017), Aug., pp. 123-138
[24] Jimenez, J., Turbulent Flows over Rough Walls, *Annu. Rev. Fluid Mech., 36* (2014), Jan., pp. 173-195
[25] Lo, K. H., *et al*., Control of Flow Seperation on a Bump by Jets in a Mach 1.9 Free-Stream: An Experimental Study, *Acta Astronautica 126* (2016), Sept.-Oct., pp. 229-242
[26] Lumley, J. L., The Structure of Inhomogeneous Turbulent Flows, in: *Atmospheric Turbulence and Radio Wave Propagation*, (Eds. A. M., Yaglom, V. I., Tatarsky), Nauka Publishing House, Moscow, Russia, 1967, pp. 166-178

[27] Sirovich, L., Turbulence and the Dynamics of Coherent Structures – Part I: Coherent Structures, *Quart. Appl. Math., 45* (1987), 3, pp. 561-571
[28] ***, Dynamic Studio User's Guide, Publication No. 9040U1859, Dantec Dynamics: Skovlunde, Denmark, 2015
[29] Prasad, B. N., Saini, J. S., Effect of Artificial Roughness on Heat Transfer and Friction Factor in a Solar Air Heater, *Solar Energy, 41* (1988), 6, pp. 555-560

Paper submitted: March 5, 2017
Paper revised: September 27, 2017
Paper accepted: September 29, 2017